Published in final edited form as:
Bone. 2013 October ; 56(2): 454–460. doi:10.1016/j.bone.2013.07.006.

Prostate Cancer Metastases Alter Bone Mineral and Matrix Composition Independent of Effects on Bone Architecture in Mice A Quantitative Study Using microCT and Raman Spectroscopy

Xiaohong Bi[a,1,*], **Julie A. Sterling**[b,c,f,g], **Alyssa R. Merkel**[b,c], **Daniel S. Perrien**[c,d,e,g], **Jeffry Nyman**[a,c,d,g], and **Anita Mahadevan-Jansen**[a]

[a]Department of Biomedical Engineering, Vanderbilt University, VU Station B#351631, 2301 Vanderbilt Place, Nashville, TN 37235, USA

[b]Department of Medicine, Division of Clinical Pharmacology, Vanderbilt University, 2200 Pierce Ave., Nashville, TN 37235, USA

[c]Vanderbilt Center for Bone Biology, Vanderbilt University, 2215B Garland Avenue, Nashville, TN 37232, USA

[d]Department of Orthopaedic Surgery and Rehabilitation, Vanderbilt University, Medical Center East, South Tower, Suite 4200, Nashville, TN 37232, USA

[e]Vanderbilt University Institute of Imaging Sciences, 1161 21st Avenue South, Medical Center North, AA-1105, Nashville, TN 37232, USA

[f]Department of Cancer Biology, Vanderbilt University, 2220 Pierce Ave., Nashville, TN 37235, USA;

[g]Tennessee Valley Healthcare System, Department of Veterans Affairs, 1310 24th AvenueSouth, Nashville, TN 37212, USA

Abstract

Prostate cancer is the most common primary tumor and the second leading cause of cancer-related deaths in men in the United States. Prostate cancer bone metastases are characterized by abnormal bone remodeling processes and result in a variety of skeletal morbidities. Prevention of skeletal complications is a crucial element in prostate cancer management. This study investigated prostate cancer-induced alterations in the molecular composition and morphological structure of metastasis-bearing bones in a mouse model of prostate cancer using Raman spectroscopy and micro-computed tomography (microCT). LNCaP C4-2B prostate cancer cells were injected into the right tibiae of 5-week old male SCID mice. Upon sacrifice at 8 weeks post tumor inoculation,

[*]Corresponding Author: Xiaohong Bi, Ph.D., Department of Nanomedicine and Biomedical Engineering, The University of Texas Health Science Center at Houston, The CABIR Building, 1881 East Road, Houston, TX 77054, USA, Xiaohong.bi@uth.tmc.edu.
[1]Present Address: Department of Nanomedicine and Biomedical Engineering, the University of Texas Health Science Center at Houston, the CABIR Building, 1881 East Road, Houston, TX 77054, USA

The authors of this paper have no conflict of interest.

DISCLOSURES

All authors state that they have no conflict of interest.

two out of the ten tumor-bearing tibiae showed only osteoblastic lesions in the radiographs, 4 osteolytic lesions only and 4 mixed with osteoblastic and osteolytic lesions.. Carbonate substitution was significantly increased while there was a marked reduction in the level of collagen mineralization, mineral crystallinity, and carbonate:matrix ratio in the cortex of the intact tumor-bearing tibiae compared to contralateral controls. MicroCT analysis revealed a significant reduction in bone volume/total volume, trabecular number and trabecular thickness, as well as significant increase in bone surface/volume ratio in tibiae with osteolytic lesions, suggesting active bone remodeling and bone loss. None of the changes in bone compositional properties were correlated with lesion area from radiographs or the changes in bone architecture from microCT. This study indicates that LNCaP C4-2B prostate cancer metastases alter bone tissue composition independent of changes in architecture, and altered bone quality may be an important contributor to fracture risk in these patients. Raman spectroscopy may provide a new avenue of investigation into interactions between tumor and bone microenvironment.

Keywords

Prostate cancer bone metastasis; bone quality; Raman spectroscopy; Osteolysis; Prostate cancer cells LNCaP C4-2B

INTRODUCTION

Prostate cancer is the most common primary tumor and the second leading cause of cancer-related deaths in men in the United States [1]. More than 80% of patients who die from advanced prostate cancer have bone metastases that cause a variety of morbidities such as bone pain, pathological fracture, hypercalcemia, and spinal cord compression [2]. Such skeletal-related events significantly impact a patient's chance of survival and quality of life. Therefore, prevention of skeletal complications is a crucial element in cancer management.

Given the clinical significance of bone metastasis, research efforts have focused on understanding the mechanisms of metastasis progression and developing therapeutic interventions using animal models of human cancer and metastasis. Assessment of tumor development and bone degeneration is important to characterize the interaction between tumor cells and the bone microenvironment as well as to evaluate the response of tissue to treatments. A variety of imaging techniques such as magnetic resonance imaging (MRI) [3], micro-positron emission tomography (PET) [4, 5], micro-computed tomography (microCT) [6], and optical imaging including bioluminescence and fluorescence imaging [7–11] have been developed to investigate cancer growth and metastasis in small animals for such purposes. Although each modality has its own specific advantages, most of the methods focus on monitoring the development and progression of tumor with limited or no information on cancer-associated changes in bone properties. Although microCT can measure the density and microarchitecture of bone tissue, it cannot examine the compositional quality of bone tissue, which may be a major determinant of bone strength and fracture risk. Hence, detailed characterization of cancer-associated alteration in bone composition, if they exist, is important to advance the understanding in tumor-bone interactions.

Vibrational spectroscopies (infrared and Raman) are ideal tools to characterize such biochemical changes because they are sensitive to molecular structure and composition in the tissue. Raman spectroscopy (RS) has additional advantages owing to its ability to analyze intact samples nondestructively and in a hydrated state. RS has previously been used in orthopedic research to assess predicted fracture risk by detecting alterations in the bone's material properties with aging or disease [12] Bone compositional properties derived from

Raman spectral parameters have been correlated with tissue-level mechanical properties [13, 14]. The decreased elastic deformation capability of aged bones associates with increasing collagen mineralization, crystallinity and carbonate substitution [15]. Fractured and unfractured osteoporotic bones showed differences in tissue composition detected by RS [16]. Specifically, iliac crest cortical bone from women with osteoporotic fractures had greater carbonate substitution in mineral structure than that from women without fractures [16]. These findings suggest that RS measurements of bone matrix composition could be important predictors of fracture risk and skeletal metabolism in other conditions including metastatic bone disease.

While numerous studies have addressed lytic and blastic architectural effects of bone metastases [17, 18] it is currently unknown whether prostate cancer metastases to bone induce changes in the composition of the bone matrix. Based on the broad spectrum of interactions known to occur between cancer and bone cells in the tumor-bone microenvironment, the present study hypothesized that Raman spectroscopy can detect cancer-induced changes in the composition of metastatic bone. Furthermore, this study sought to determine whether metastatic effects on bone composition were independent of metastatic effects on bone architecture. A mouse model of prostate cancer was used to produce mixed osteoblastic and osteolytic lesions that mimic human prostate cancer bone metastases. Bone composition and architecture from the tumor-bearing tibiae and the contralateral controls were quantitatively characterized using RS and microCT, respectively.

MATERIALS AND METHODS

Animal study

All procedures were performed in compliance with Vanderbilt University Institutional Animal Care and Use Committee and National Institutes of Health guidelines. The LNCaP C4-2B prostate cancer cells (100,000 cells in 10 μl) were injected into the right tibiae of 5-week-old male, severe combined immunodeficiency (SCID) mice (Harlan Sprague Dawley, n = 10), while the left tibiae were injected with phosphate buffered saline (PBS) as contralateral control (n = 10). Another parallel control group of SCID mice received vehicle injection in the right tibiae and no treatment in the left side (n = 10). The injection procedure was performed under anesthesia using previously reported methods.[19, 20] Briefly, the hind limbs were treated with depilatory cream for hair removal. After disinfection with Betadine and alcohol wipes at the knee area, a 27-gauge needle was inserted ~3 mm into the proximal end of the tibiae by twisting through the cortical bone in a drilling motion, and the cancer cells or PBS were then injected. The procedure was performed on 5-week-old mice with an open growth plate to reduce the osseous blockage during injection. After tumor induction, animals were treated with one dose of analgesic Buprenex subcutaneously at 2.5mg/kg body weight, and were monitored daily for discomfort and pain in the first 3 days after injection. All mice were sacrificed at 8 weeks post tumor induction when bone lesions were evident on the radiographs. All the tumorous, contralateral and control tibiae were harvested, cleaned of excess soft tissue, and stored in 70% alcohol at a 4 °C before microCT and Raman measurements.

Digital radiographs were acquired weekly in vivo from the tumor-bearing mice starting 4 weeks after injection to monitor lesion development. With an exposure energy of 35 kVp for 8 seconds, plane radiographs were acquired while the mice were lying in a prone position under anesthesia using a XR-60 digital radiography system (Faxitron). All radiographs were evaluated in a blinded fashion. The number and area of osteolytic and osteoblastic bone metastases were calculated on radiographs using MetaMorph, a computerized image analysis system (Molecular Devices, Inc.) [21, 22].

MicroCT

The types of tumor-induced lesions (osteolytic, osteoblastic, or both) present in tibial metaphysis and the effect of the tumor on mineralization, cortical and trabecular architecture were determined using micro computed tomography. Cross-sectional images of the proximal tibia were acquired *ex vivo* using a μCT40 (Scanco Medical, Brüttisellen Switzerland). The region of interest including the metaphysis and mid-diaphysis of tibia was identified from a 'scout' scan of each bone prior to image acquisition. The region was scanned at an isotropic voxel size of 12 μm with X-ray source settings at 70 kVp and 145mA, 250 projections per 180°, and an integration time of 300 ms. Bone was segmented from soft tissue using a threshold of 411 mg HA/ccm, Sigma 0.2 and Support of 1. The cortical bone volume and mean cortical thickness were quantified from the mid-diaphysis using Scanco evaluation software. Trabecular bone volume and architecture in the proximal metaphysis were calculated as previously described [23], including bone volume fraction (BV/TV), trabecular number (Tb.N), and trabecular thickness (Tb.Th). Bone tissue mineral density (TMD) and bone surface to volume ratio (BS/BV) were also determined from the tumor-bearing tibiae and the contralateral tibiae without tumor.

Raman spectroscopy measurement

Following microCT analysis, Raman measurements of the periosteal surface of intact host cortical bone at the tibial metaphysis were carried out using a confocal Raman microscope (Renishaw, Ramascope Mark III), which couples a Raman spectrometer to a confocal microscope, a CCD detector, and a diode laser emitting at 785 nm. The intact tibiae were mounted on a microscope slide using mold polymer clay, with the surface of the proximal metaphysis leveled horizontally. The 785 nm laser light was focused to the metaphysis of tibiae through the Leica 50X N Plan (NA = 0.75) lens with a laser power of 30mw on sample and laser spot size ~3–4 μm in diameter. Three spectra were collected from the host cortical bone of proximal tibia metaphysis (schemed in Figure 1). Each spectrum consisted of three accumulations with an exposure time of 10 seconds, a binning of 3 and spectral resolution of 3 cm^{-1}.

Custom scripts written in Matlab were used to correct the baseline of each spectrum and to calculate the compositional properties. Peak intensities of Raman signatures from mineral and collagen were determined, including phosphate v1 (960 cm^{-1}), carbonate (1070 cm^{-1}), proline (856 cm^{-1}), hydroxyproline (876 cm^{-1}) and amide 1 (1665 cm^{-1}) [14, 24].

Statistical analysis

Statistical analysis was performed using SigmaPlot 12 software (Systat Software, Chicago, IL, USA). The statistical significance of tumor-associated changes in microCT and Raman spectral measures was tested using paired Student's *t*-tests on the tumor-bearing tibiae and the contralateral controls, and using One-way ANOVA for comparing the tumor group and all the control groups. The significance level was set at $p < 0.05$.

RESULTS

Raman spectra vary between tumor and non-tumor bearing bones

Representative digital radiographs from a tumor-bearing tibia and the contralateral non-tumor bearing control are shown in Figure 1.A–B. Raman spectra were collected from the cortical bone of proximal tibia metaphysis as indicated by the red dots on Figure 1.D. Mean Raman spectra from the tumor and non-tumor tibiae were overlaid to demonstrate the variation in major bone components (Figure 1.C). Raman signatures from bone mineral and organic matrix including phosphate, carbonate, proline, hydroxyproline and collagen amide 1 are labeled on the graph. Variations in the intensities of multiple Raman bands indicate

differences in the content and organization of the assigned molecules. Since proline is one of the major amino acids in collagen, its peak height has been used to calculate the abundance of collagen, representing the same molecular composition as the collagen amide 1 band.

Cancer induces bone compositional changes

Raman spectral parameters of mineral and matrix composition were compared between tumor bearing tibiae and the contralateral control of each animal to assess tumor effects on host cortical bone composition. Figure 2 shows the compositional properties of tumor bearing tibiae in ratio to the contralateral controls. Tumor-associated percent changes in all the Raman measures were illustrated in Table 1. The degree of collagen mineralization, calculated by taking the peak height ratio of phosphate v1/proline or phosphate v1/amide 1, reduced 41.2% (± 13.6%) and 46.8% (± 22.0%) with tumor, respectively ($p < 0.01$). Hydroxyapatite crystallinity was determined by the reciprocal of full width at half maximum (FWHM) of phosphate v1, and demonstrated a significant decrease in the cortex of tumor-bearing bone by an average of 3.9% (± 4.1%) ($p < 0.01$). The type B carbonate substitution level (carbonate/phosphate v1) was 10.6% (± 7.3%) greater in tumor-bearing bones ($p < 0.01$), suggesting higher mineral carbonation rate. The presence of prostate tumors also decreased the carbonate:matrix ratio by 36.3% (± 13.1%) when calculated as carbonate/proline ($p < 0.01$) and 43.1% (± 22.1%) when calculated as carbonate/amide 1 ($p < 0.01$, Table 1).

Bone lesions present in all the tibiae inspected by radiographs

The intra-tibial injection of LNCaP C4-2B cancer cells has previously been reported to yield mixed lesions [25] making this model consistent with clinical observation of prostate cancer metastasis to bone. In the current study, the radiographs indicated that two out of the ten tumor-bearing tibiae had primarily osteoblastic lesions, 4 primarily had osteolytic lesions and 4 had a mix of osteoblastic and osteolytic lesions, consistent with literature reports. Representative images are shown in Figure 1.B1-3. Further inspection of inspection of the lesions by microCT revealed that three out of the ten tibiae showed primarily local osteoblatic lesions at the metaphysis (P1) where the Raman spectra were collected, while 7 tibiae demonstrated osteolytic lesions at P1. The osteolytic lesion area was calculated for all bones with either mixed osteoblastic-osteolytic or only osteolytic activity in the whole tibiae. The compositional changes detected by RS in these tumor-bearing tibiae did not correlate with whole bone osteolytic lesion area, suggesting that the observed changes in host bone composition may not be related to total osteoclastic activity. However, the osteolytic area at P1 demonstrated a non-statistically significant negative association with carbonate:matrix ratio ($p = 0.10$) and mineral crystallinity ($p = 0.12$) with the current sample size.

Bone loss is detected by microCT in the osteolytic tumor-bearing bones

The architectural properties of tibial metaphysis were evaluated using microCT (Figure 3). The seven tumor-bearing tibiae that showed predominant osteolytic lesions at P1 (metaphysis) in the radiograph were analyzed to quantitatively confirm the expected loss of bone volume. A marked decrease was observed in bone volume fraction (Figure 3.A, $p < 0.05$), trabecular number (Figure 3.B, $p < 0.05$) and trabecular thickness (Figure 3.C, $p < 0.05$), confirming bone loss and architectural destruction. Bone surface/volume ratio (BS/BV) in Figure 3.D demonstrated a significant increase with the presence of tumor, consistent with thinning of the bony structures. The mean volumetric tissue mineral density (TMD) of the mineralized tissue was quantified for the trabecular and cortical regions. No significant changes in TMD were observed between non- tumor bearing bone and tumor bearing bones with either the mixed lesions or the osteolytic lesions alone (Table 1), indicating that RS is more sensitive than microCT in detecting cancer-induced changes in mineral phase.

Observed structural changes are independent of damage caused by tibial injection

Intratibial injections cause physical damage to the epiphysis, growth plate, and trabecular bone, and result in partial marrow ablation, which alter bone remodeling in the absence of tumor cells. Hence the injection procedure alone could be responsible for the observed changes in bone composition. To address this question, the contralateral control (C) in tumor-bearing mice were compared with the vehicle injection control (V.C) and non-injection control (N.C.) tibiae in the control group. Mean values for the spectral parameters that differentiate the tumor-bearing tibiae with the contralateral tibiae were calculated and compared across all the four groups (Figure 4). The tumor-bearing bones showed significant difference in bone mineral and matrix composition, consistent with the outcome from paired comparison. No significant differences in bone composition were observed between the injection controls in tumor-bearing or non-tumor bearing mice, suggesting the observed structural changes with tumor are caused by tumor presence in the bone and are independent of the damage caused by injection. Furthermore, similarity of RS between the injection control bones of mice bearing tumors in contralateral leg, and those not injected in the contralateral leg, suggests that tumor-derived systemic factors/effects do not alter bone matrix properties. A paired t-test of compositional properties between PBS-injected and non-injected tibiae from the non-tumor-bearing mice demonstrated a significant decrease in collagen mineralization (phosphate v1/proline), mineral crystallinity, as well as carbonate/matrix ratio (carbonate/proline) in the injection control tibiae (Figure 5), consistent with the known effects of intra-tibial injection through the growth plate on bone remodeling and development.

DISCUSSION

In this study, we examined whether the physicochemical and compositional properties of preexisting host cortical bone change with the presence of prostate tumor, which could provide a new measure to understand bone-tumor interactions. Therefore, Raman spectroscopic analysis was conducted to characterize prostate cancer-induced variations in molecular structure and composition of metastatic bones. A significant reduction in the level of collagen mineralization, mineral crystallinity and carbonate:matrix ratio, as well as an increase in carbonation were observed in the cortex of tumor-bearing tibiae. The compositional changes were accompanied by the expected architectural deterioration in bone structure and morphological bone degeneration, observed by microCT and radiography.

Prostate cancer bone metastases are characterized by substantial localized osteolysis and the replacement of lamellar structure with woven bone [26]. Both bone resorption and formation processes are markedly enhanced as shown by elevated serum and urinary biomarkers of bone turnover [27]. The microCT analysis in this study revealed bone structural changes that agreed with previous studies reporting the effects of prostate tumors on bone [28–30]. There were however, no differences in microCT-derived TMD between the tumor-bearing and non-tumor-bearing bones also as reported in prostate cancer investigations [28–30]. In contrast, bone composition such as the degree of collagen mineralization detected by RS showed consistent changes with the presence of tumor regardless of the lesion type in this study, indicating that RS is a more sensitive method to probe the biochemical properties of bone tissue than microCT.

The mineral in bone is calcium phosphate in an apatite structure, with ~5–8 wt% of carbonate content [31, 32]. The major species of carbonation is in the form of type B carbonate substitution, where PO_4^{3-} is substituted by CO_3^{2-}. Carbonate substitution rate, calculated by the peak height (or area) ratio of carbonate:phosphate v1, is an important spectral parameter associated with tissue maturity and age. Carbonation level increases

sharply in newly formed bone during maturation [33–35], and appears to increase further with aging in human and animals [15, 35–38]. Type B carbonate content in an aged rat model was reported to be 17% and 10% greater than that of young and middle-aged rats, respectively [15]. The enhanced carbonation of the mineral lattice has been hypothesized to result from the elevated systemic acidity in the skeleton with aging [37, 39, 40]. The current study revealed that type B carbonate content increased in all the tumor-bearing bones with osteolytic or osteoblastic lesions.

Resorption of bone mineral occurs through the acidification of the extracelluar compartment within the osteoclast-bone interface. This osteoclast-mediated process involves release of protons for acidification and possibly exchange of HCO_3^-/Cl^- to maintain the cytoplasmic pH homeostasis [41]. The enhanced activation of osteoclasts in bone metastases likely elevates the abundance of protons and HCO_3^- in bone microenvironment, which favors the carbonation reaction throughout bone matrix as fluid flows through the cannilicular system in the cortex. In addition, the acidic pH in the extracellular fluid of tumor [42–44] might cause an acid-base imbalance in the bone microenvironment, resulting in increased carbonate content in tumor-bearing bones.

Similar to the carbonation parameter (carbonate-to-phosphate), the carbonate-to-matrix ratio also provides valuable information about the tissue's material properties, and varies with disease [45], menopausal status [46], fracture history [16, 47], and therapeutic treatment [46, 48, 49]. In the present study this spectral parameter showed strong correlation with the degree of collagen mineralization ($p < 0.001$, $R^2 = 1.00$), indicating a strong relationship with the remodeling activity in the tissue. This result is in agreement with a previous report by Isaksson et al. where carbonate-to-amide 1 (or phosphate) ratio showed a significant negative correlation with histomorphometric parameters related to bone remodeling and turnover rate [45]. In bones with prostate cancer cells, carbonate-to-phosphate ratio significantly increased while carbonate-to-matrix ratio diminished, suggesting that decreased carbonate-to-matrix value arises from elevated bone turnover rate instead of a synergetic change with mineralization.

Mineral crystallinity has been correlated with mineral crystal size and the stoichiometric perfection of crystal structure [50]. As carbonate level increases, more carbonate ions occupy the stoichiometric phosphate locations, which results in a reduction in the crystallinity or perfection of the hydroxyapatite crystals. Significant negative correlations have been shown between carbonate content and crystallinity [37, 51]. This is consistent with reduced mineral crystallinity and increased carbonation in tumor-bearing bones from the current study.

The osseous prostate cancer model in the present study yields mixed osteoblastic/osteolytic lesions, which commonly occur in prostate cancer patients. RS-derived bone compositional properties demonstrated consistent variations in the tumor-bearing tibiae despite the lesion types present in the region of the bone where RS measurements were collected, indicating that the tumor, rather than lytic or blastic processes, induced compositional changes in the host cortical bone. Future studies on solely osteolytic or osteoblastic animal models will help illustrate the effect of other tumors and distinctive types of lesions.

In conclusion, the interaction between tumor and the bone microenvironment leads to increased bone turnover, which results in marked changes in the material properties of bone tissue. These alterations are independent of the lesion area from radiographs or the architecture changes from microCT analysis, suggesting that RS could provide additional information in the assessment of metastatic bone disease at the molecular level. Although the present study investigated bone samples ex vivo, it found that RS can be capable of

characterizing tumor-bearing bone and provides impetus for future RS technique development to detect subsurface bone metastasis in vivo. Spatially Offset Raman Spectroscopy (SORS) is one such method that can make deep tissue RS measurement by spatially separating the illumination source and the detection elements [52]. Raman signatures of buried bone have been non-invasively detected through several millimeters of soft tissue from cadavers and tibiae of small animals using SORS[53–55]. It is expected that the development of SORS method will allow for non-invasive in vivo detection of cancer-associated changes in bone composition that could contribute to fracture risk independent of reduced bone volume and architectural degradation.

Acknowledgments

The authors thank Barbara Rowland for assistance in harvesting tibiae from the mice and would like to acknowledge the support from of Biomedical Photonics Center and the Center for Bone Biology at Vanderbilt University. This study was supported by K25 National Institute of Health grant K25CA149194-01 (XB), VA Career Development Award (JAS), Vanderbilt Breast Spore P50CA098131 (XB, JAS, and JSN), and the Vanderbilt Center for Bone Biology Program Project P01CA40035 (XB, JAS, DSP, and JSN).

References

1. Surveillance, E., and End Results (SEER) Program and the National Cancer for Health Statistics. SEER Stat Fact Sheets: Prostate. 2012. Available from: http://seer.cancer.gov/statfacts/html/prost.html
2. Mundy GR. Metastasis to bone: causes, consequences and therapeutic opportunities. Nat Rev Cancer. 2002; 2(8):584–93. [PubMed: 12154351]
3. Rozel S, Galban CJ, Nicolay K, Lee KC, Sud S, Neeley C, Snyder LA, Chenevert TL, Rehemtulla A, Ross BD, Pienta KJ. Synergy between anti-CCL2 and docetaxel as determined by DW-MRI in a metastatic bone cancer model. J Cell Biochem. 2009; 107(1):58–64. [PubMed: 19259948]
4. Hsu WK, Virk MS, Feeley BT, Stout DB, Chatziioannou AF, Lieberman JR. Characterization of osteolytic, osteoblastic, and mixed lesions in a prostate cancer mouse model using 18F-FDG and 18F-fluoride PET/CT. J Nucl Med. 2008; 49(3):414–21. [PubMed: 18287261]
5. Hong H, Zhang Y, Sun J, Cai W. Positron emission tomography imaging of prostate cancer. Amino Acids. 2010; 39(1):11–27. [PubMed: 19946787]
6. Johnson LC, Johnson RW, Munoz SA, Mundy GR, Peterson TE, Sterling JA. Longitudinal live animal micro-CT allows for quantitative analysis of tumor-induced bone destruction. Bone. 2011; 48:141–51. [PubMed: 20685406]
7. Drake JM, Gabriel CL, Henry MD. Assessing tumor growth and distribution in a model of prostate cancer metastasis using bioluminescence imaging. Clin Exp Metastasis. 2005; 22(8):674–84. [PubMed: 16703413]
8. Hsieh CL, Xie Z, Yu J, Martin WD, Datta MW, Wu GJ, Chung LW. Non-invasive bioluminescent detection of prostate cancer growth and metastasis in a bigenic transgenic mouse model. Prostate. 2007; 67(7):685–91. [PubMed: 17342752]
9. Hoffman R. Green fluorescent protein imaging of tumour growth, metastasis, and angiogenesis in mouse models. Lancet Oncol. 2002; 3(9):546–56. [PubMed: 12217792]
10. Burton DW, Geller J, Yang M, Jiang P, Barken I, Hastings RH, Hoffman RM, Deftos LJ. Monitoring of skeletal progression of prostate cancer by GFP imaging, X-ray, and serum OPG and PTHrP. Prostate. 2005; 62(3):275–81. [PubMed: 15389781]
11. Kaijzel EL, Snoeks TJ, Buijs JT, van der Pluijm G, Lowik CW. Multimodal imaging and treatment of bone metastasis. Clin Exp Metastasis. 2009; 26(4):371–9. [PubMed: 18941911]
12. Morris M, Mandair G. Raman assessment of bone quality. Clinical orthopaedics and related research. 2011; 469(8):2160–2169. [PubMed: 21116756]
13. Bi X, Nyman JS, Patil CA, Masui P, Lynch C, Mahadevan-Jansen A. Raman spectroscopy for assessment of bone quality in MMP-2 knockout mice. Proc SPIE. 2009:7166.

14. Bi X, Patil CA, Lynch C, Pharr G, Mahadevan-Jansen A, Nyman J. Raman and mechanical properties correlate at whole bone- and tissue-levels in a genetic mouse model. Journal of biomechanics. 2011; 44(2):297–303. [PubMed: 21035119]
15. Akkus O, Polyakova-Akkus A, Adar F, Schaffler MB. Aging of microstructural compartments in human compact bone. J Bone Miner Res. 2003; 18(6):1012–9. [PubMed: 12817753]
16. McCreadie BR, Morris MD, Chen TC, Sudhaker Rao D, Finney WF, Widjaja E, Goldstein SA. Bone tissue compositional differences in women with and without osteoporotic fracture. Bone. 2006; 39(6):1190–5. [PubMed: 16901772]
17. Sone T, Tamada T, Jo Y, Miyoshi H, Fukunaga M. Analysis of three-dimensional microarchitecture and degree of mineralization in bone metastases from prostate cancer using synchrotron microcomputed tomography. Bone. 2004; 35(2):432–438. [PubMed: 15268894]
18. Tamada T, Sone T, Jo Y, Imai S, Kajihara Y, Fukunaga M. Three-dimensional trabecular bone architecture of the lumbar spine in bone metastasis from prostate cancer: comparison with degenerative sclerosis. Skeletal Radiol. 2005; 34(3):149–55. [PubMed: 15723255]
19. Corey E, Quinn JE, Bladou F, Brown LG, Roudier MP, Brown JM, Buhler KR, Vessella RL. Establishment and characterization of osseous prostate cancer models: intra-tibial injection of human prostate cancer cells. Prostate. 2002; 52(1):20–33. [PubMed: 11992617]
20. Campbell JP, Merkel AR, Masood-Campbell SK, Elefteriou F, Sterling JA. Models of bone metastasis. J Vis Exp. 2012; (67):e4260. [PubMed: 22972196]
21. Guise TA, Yin JJ, Taylor SD, Kumagai Y, Dallas M, Boyce BF, Yoneda T, Mundy GR. Evidence for a causal role of parathyroid hormone-related protein in the pathogenesis of human breast cancer-mediated osteolysis. J Clin Invest. 1996; 98(7):1544–9. [PubMed: 8833902]
22. Yin JJ, Selander K, Chirgwin JM, Dallas M, Grubbs BG, Wieser R, Massague J, Mundy GR, Guise TA. TGF-beta signaling blockade inhibits PTHrP secretion by breast cancer cells and bone metastases development. J Clin Invest. 1999; 103(2):197–206. [PubMed: 9916131]
23. Perrien D, Akel N, Edwards P, Carver A, Bendre M, Swain F, Skinner R, Hogue W, Nicks K, Pierson T, Suva L, Gaddy D. Inhibin A is an endocrine stimulator of bone mass and strength. Endocrinology. 2007; 148(4):1654–1665. [PubMed: 17194739]
24. Bi X, Patil C, Morrissey C, Roudier M, Mahadevan-Jansen A, Nyman J. Characterization of bone quality in prostate cancer bone metastases using Raman spectroscopy. Proc SPIE. 2010; 7458(F): 183.
25. Li X, Sterling JA, Fan KH, Vessella RL, Shyr Y, Hayward SW, Matrisian LM, Bhowmick NA. Loss of TGF-beta responsiveness in prostate stromal cells alters chemokine levels and facilitates the development of mixed osteoblastic/osteolytic bone lesions. Mol Cancer Res. 2012; 10(4):494–503. [PubMed: 22290877]
26. Clarke NW I, Holbrook B, McClure J, George NJ. Osteoclast inhibition by pamidronate in metastatic prostate cancer: a preliminary study. Br J Cancer. 1991; 63(3):420–3. [PubMed: 2003984]
27. Roato I, D'Amelio P, Gorassini E, Grimaldi A, Bonello L, Fiori C, Delsedime L, Tizzani A, De Libero A, Isaia G, Ferracini R. Osteoclasts are active in bone forming metastases of prostate cancer patients. PLoS One. 2008; 3(11):e3627. [PubMed: 18978943]
28. Fritz V, Louis-Plence P, Apparailly F, Noël D, Voide R, Pillon A, Nicolas JC, Müller R, Jorgensen C. Micro-CT combined with bioluminescence imaging: a dynamic approach to detect early tumor-bone interaction in a tumor osteolysis murine model. Bone. 2007; 40:1032–1072. [PubMed: 17251073]
29. Johnson L, Johnson R, Munoz S, Mundy G, Peterson T, Sterling J. Longitudinal live animal micro-CT allows for quantitative analysis of tumor-induced bone destruction. Bone. 2011; 48(6ce53b87-e546–3607-d975-ddec692bb144):141–192. [PubMed: 20685406]
30. Wan X, Li ZG, Yingling J, Yang J, Starbuck M, Ravoori M, Kundra V, Vazquez E, Navone N. Effect of transforming growth factor beta (TGF-β) receptor I kinase inhibitor on prostate cancer bone growth. Bone. 2012; 50:695–1398. [PubMed: 22173053]
31. Penel G, Leroy G, Rey C, Bres E. MicroRaman spectral study of the PO4 and CO3 vibrational modes in synthetic and biological apatites. Calcif Tissue Int. 1998; 63(6):475–81. [PubMed: 9817941]

32. Awonusi A, Morris MD, Tecklenburg MM. Carbonate assignment and calibration in the Raman spectrum of apatite. Calcif Tissue Int. 2007; 81(1):46–52. [PubMed: 17551767]
33. Tarnowski CP, Ignelzi MA Jr, Morris MD. Mineralization of developing mouse calvaria as revealed by Raman microspectroscopy. J Bone Miner Res. 2002; 17(6):1118–26. [PubMed: 12054168]
34. Fuchs RK, Allen MR, Ruppel ME, Diab T, Phipps RJ, Miller LM, Burr DB. In situ examination of the time-course for secondary mineralization of Haversian bone using synchrotron Fourier transform infrared microspectroscopy. Matrix Biol. 2008; 27(1):34–41. [PubMed: 17884405]
35. Donnelly E, Boskey AL, Baker SP, van der Meulen MC. Effects of tissue age on bone tissue material composition and nanomechanical properties in the rat cortex. J Biomed Mater Res A. 2010; 92(3):1048–56. [PubMed: 19301272]
36. Burnell JM, Teubner EJ, Miller AG. Normal maturational changes in bone matrix, mineral, and crystal size in the rat. Calcif Tissue Int. 1980; 31(1):13–9. [PubMed: 6770970]
37. Yerramshetty JS, Lind C, Akkus O. The compositional and physicochemical homogeneity of male femoral cortex increases after the sixth decade. Bone. 2006; 39(6):1236–43. [PubMed: 16860007]
38. Burket J, Gourion-Arsiquaud S, Havill LM, Baker SP, Boskey AL, van der Meulen MC. Microstructure and nanomechanical properties in osteons relate to tissue and animal age. J Biomech. 2011; 44(2):277–84. [PubMed: 21074774]
39. Bushinsky DA. Acid-base imbalance and the skeleton. Eur J Nutr. 2001; 40(5):238–44. [PubMed: 11842949]
40. Arnett T. Regulation of bone cell function by acid-base balance. Proc Nutr Soc. 2003; 62(2):511–20. [PubMed: 14506899]
41. Rousselle AV, Heymann D. Osteoclastic acidification pathways during bone resorption. Bone. 2002; 30(4):533–40. [PubMed: 11934642]
42. Griffiths JR. Are cancer cells acidic? Br J Cancer. 1991; 64(3):425–7. [PubMed: 1911181]
43. Gatenby RA, Gawlinski ET, Gmitro AF, Kaylor B, Gillies RJ. Acid-mediated tumor invasion: a multidisciplinary study. Cancer Res. 2006; 66(10):5216–23. [PubMed: 16707446]
44. Yoneda T, Hata K, Nakanishi M, Nagae M, Nagayama T, Wakabayashi H, Nishisho T, Sakurai T, Hiraga T. Involvement of acidic microenvironment in the pathophysiology of cancer-associated bone pain. Bone. 2011; 48(1):100–5. [PubMed: 20637323]
45. Isaksson H, Turunen MJ, Rieppo L, Saarakkala S, Tamminen IS, Rieppo J, Kroger H, Jurvelin JS. Infrared spectroscopy indicates altered bone turnover and remodeling activity in renal osteodystrophy. J Bone Miner Res. 2010; 25(6):1360–6. [PubMed: 20200925]
46. Huang RY, Miller LM, Carlson CS, Chance MR. Characterization of bone mineral composition in the proximal tibia of cynomolgus monkeys: effect of ovariectomy and nandrolone decanoate treatment. Bone. 2002; 30(3):492–7. [PubMed: 11882463]
47. Tamminen IS, Mayranpaa MK, Turunen MJ, Isaksson H, Makitie O, Jurvelin JS, Kroger H. Altered bone composition in children with vertebral fracture. J Bone Miner Res. 2011; 26(9): 2226–34. [PubMed: 21509822]
48. Boskey AL, Spevak L, Weinstein RS. Spectroscopic markers of bone quality in alendronate-treated postmenopausal women. Osteoporos Int. 2009; 20(5):793–800. [PubMed: 18769963]
49. Garip S, Severcan F. Determination of simvastatin-induced changes in bone composition and structure by Fourier transform infrared spectroscopy in rat animal model. J Pharm Biomed Anal. 2010; 52(4):580–8. [PubMed: 20185263]
50. Yerramshetty JS, Akkus O. The associations between mineral crystallinity and the mechanical properties of human cortical bone. Bone. 2008; 42(3):476–82. [PubMed: 18187375]
51. Ou-Yang H, Paschalis EP, Mayo WE, Boskey AL, Mendelsohn R. Infrared microscopic imaging of bone: spatial distribution of CO3(2-). J Bone Miner Res. 2001; 16(5):893–900. [PubMed: 11341334]
52. Matousek P I, Clark P, Draper ER, Morris MD, Goodship AE, Everall N, Towrie M, Finney WF, Parker AW. Subsurface probing in diffusely scattering media using spatially offset Raman spectroscopy. Appl Spectrosc. 2005; 59(4):393–400. [PubMed: 15901323]

53. Schulmerich MV, Dooley KA, Morris MD, Vanasse TM, Goldstein SA. Transcutaneous fiber optic Raman spectroscopy of bone using annular illumination and a circular array of collection fibers. J Biomed Opt. 2006; 11(6):060502. [PubMed: 17212521]

54. Schulmerich MV, Cole JH, Kreider JM, Esmonde-White F, Dooley KA, Goldstein SA, Morris MD. Transcutaneous Raman spectroscopy of murine bone in vivo. Appl Spectrosc. 2009; 63(3): 286–95. [PubMed: 19281644]

55. Okagbare PI, Begun D, Tecklenburg M, Awonusi A, Goldstein SA, Morris MD. Noninvasive Raman spectroscopy of rat tibiae: approach to in vivo assessment of bone quality. J Biomed Opt. 2012; 17(9):90502–1. [PubMed: 23085899]

Highlights

1. Increased carbonate substitution in hydroxyapatite mineral structure with tumor
2. Decreased collagen mineralization, mineral crystallinity, carbonate:matrix ratio with tumor
3. Significant changes in bone architecture but not tissue bone mineral density with tumor
4. Prostate cancer induced compositional changes are independent of the architecture alterations.

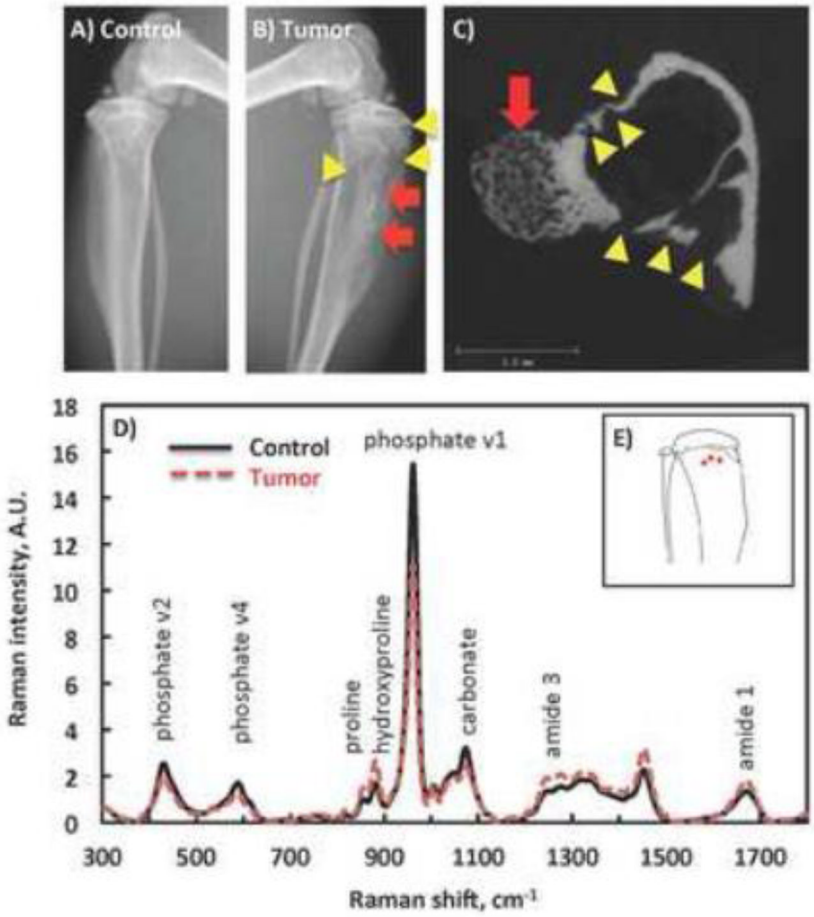

Figure 1.

Osteoblastic and osteolytic lesions are show in representative radiographs from a PBS-injected, non-tumor-bearing contralateral control (A) and a prostate tumor-bearing tibia (B), and a representative cross sectional microCT image from the tibial metaphysis. A mixture of osteolytic lesions (yellow arrow heads) and osteoblastic lesions (red arrows) are easily distinguishable in both the radiograph and microCT images which were used to characterize the predominance of these lesion types in each specimen. C) Mean Raman spectra from the tumor-bearing tibiae (dashed line) and the contralateral controls (solid line). Selective Raman bands were marked with biochemical assignments. D) Illustration of Raman spectra collection spots (red dots) on the cortex of mouse tibia.

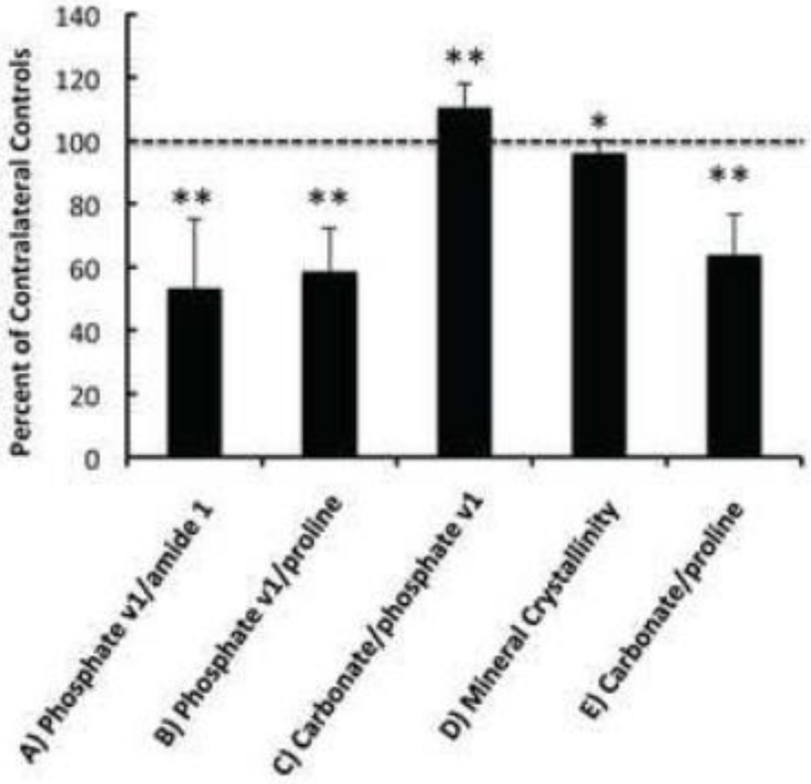

Figure 2.

Raman-derived parameters of bone compositions in tumor bearing tibiae in ratio to the values from the contralateral controls. Dashed line marks the relative level of all the control spectral components, or 100%. Compositional properties shown include the level of collagen mineralization calculated by phosphate v1/amide 1 (A) and phosphate v1/proline (B), carbonate substitution in hydroxyapatite by carbonate/phosphate v1 (C), mineral crystallinity by 1/FWHM of phosphate v1 (D), and carbonate:matrix ratio by carbonate/proline (E). All spectral parameters in Figure 2.A–E demonstrate statistically significant difference with the contralateral controls (**$p<0.01$, *$p < 0.05$).

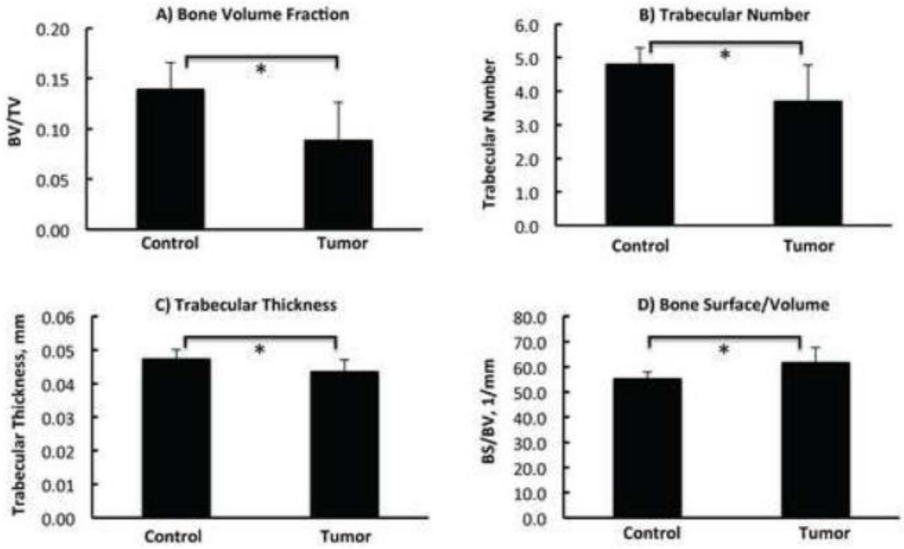

Figure 3.

Comparison of bone architecture from microCT analysis between the contralateral control and the tumor-bearing tibiae with osteolytic lesions (n=7). The bone volume fraction (BV/TV) (A), trabecular number (B), trabecular thickness (C) and bone surface/volume (D) were compared. Statistical significant difference was observed for Figure 3.A–D. Asterisk sign (*) represents $p<0.05$.

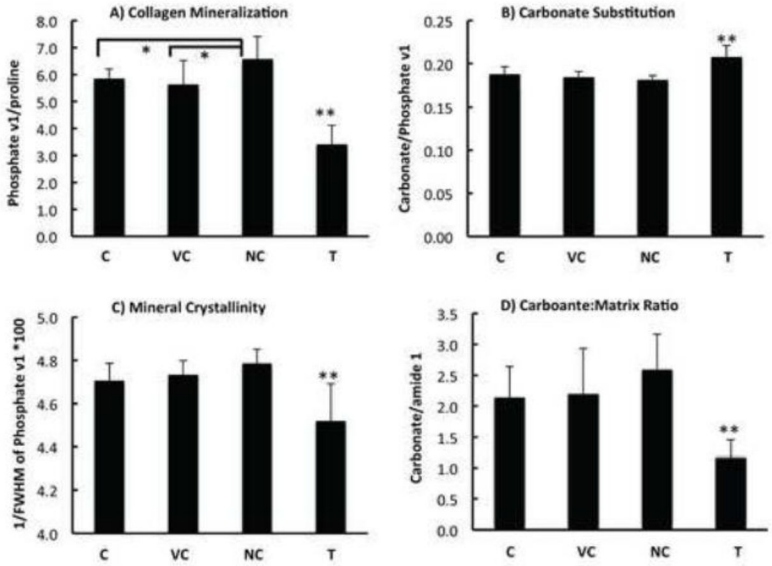

Figure 4.

Raman-derived bone compositions in tumor-bearing tibiae (T) compared with contralateral control (C), vehicle injection control (V.C), and non-injection control (N.C). The level of collagen mineralization (A), carbonate substitution in hydroxyapatite (B), mineral crystallinity (C), and carbonate:matrix ratio (D) from tumor group are significantly different with all the control groups. Double asterisk (**) and asterisk signs (*) represent $p < 0.01$ and $p < 0.05$, respectively.

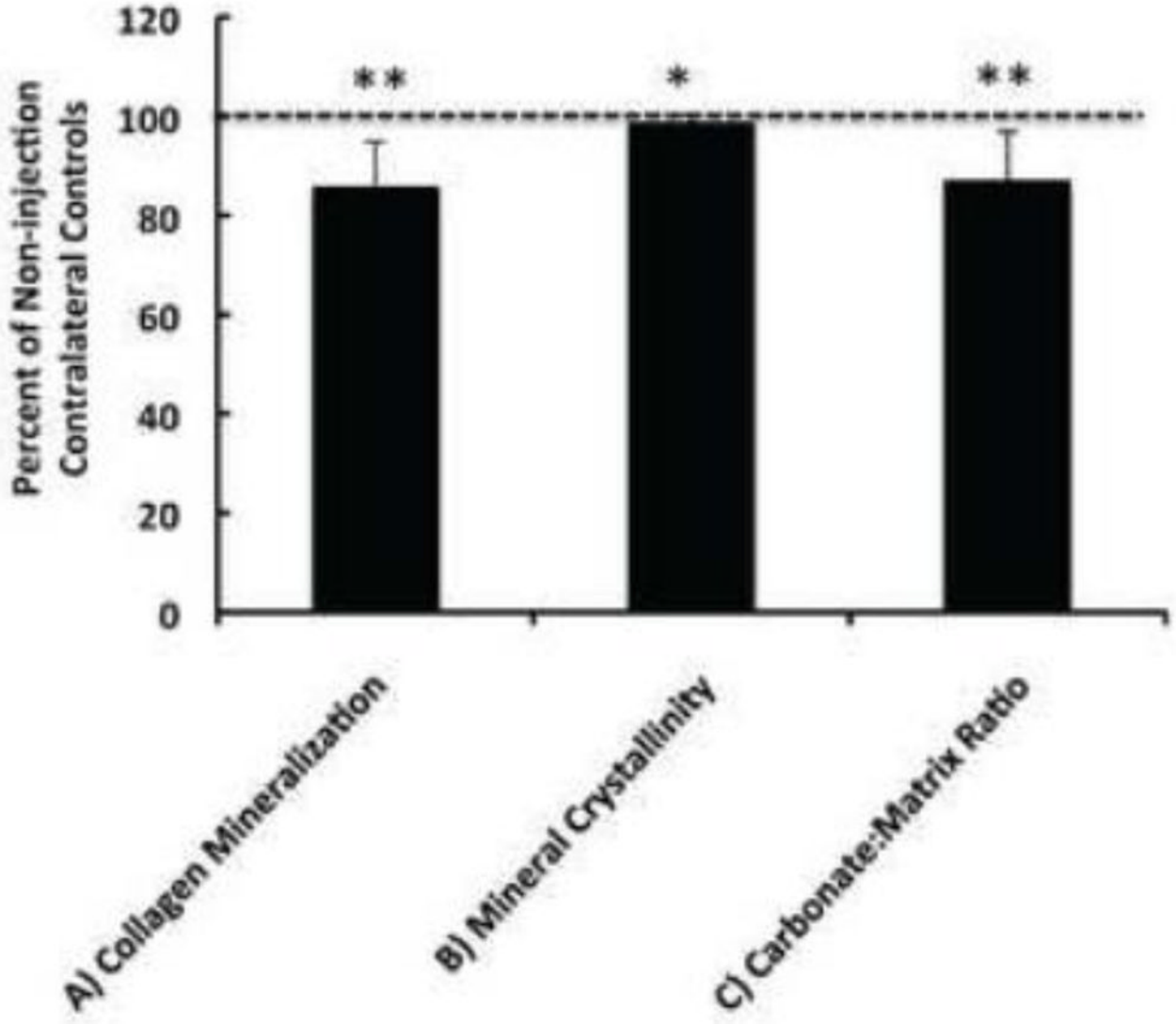

Figure 5.

Bone compositional properties of injection controls from non-tumor bearing mice in ratio to the values from the contralateral non-injection controls. Dashed line marks the relative level of each spectral parameter from the contralateral controls, or 100%. Compositional properties shown include the level of collagen mineralization calculated by phosphate v1/proline (A), mineral crystallinity by 1/FWHM of phosphate v1 (B), and carbonate:matrix ratio by carbonate/proline (C). All spectral parameters in Figure 5.A–C demonstrate statistically significant difference with the contralateral non-injection controls (**$p<0.01$; *$p < 0.05$).

Table 1

Summary of cancer-induced changes in bone composition and architecture. Changes in Raman spectral parameters were universal in all the mice (n = 10). The microCT measures were calculated from the mice with osteolytic lesions only (n = 7).

Raman Measure	% change, Mean (SD)	microCT Measure	% change, Mean (SD)
Phosphate/amide 1	−46.8 (22.0) **	BV/TV	−30.4 (32.1) *
Phosphate/proline	−41.2 (13.6) **	Trabecular Number	−12.1 (18.3) *
Carbonate/phosphate	10.6 (7.3) **	Trabecular Thickness	−8.9 (11.3) *
Carbonate/proline	−36.3 (13.1) **	BS/BV	15.8 (12.0) *
Mineral crystallinity	−3.9 (4.1) **	TMD	0.1 (5.4)

* $p < 0.05$;

** $p < 0.01$